Acta Materialia 200 (2020) 932–942

Contents lists available at ScienceDirect

Acta Materialia

journal homepage: www.elsevier.com/locate/actamat

Full length article

First principles study of the effect of hydrogen in austenitic stainless steels and high entropy alloys

Xiao Zhou*, William A. Curtin

Laboratory for Multiscale Mechanics Modeling, EPFL, Lausanne CH-1015, Switzerland

ARTICLE INFO

Article history:
Received 27 May 2020
Revised 19 August 2020
Accepted 16 September 2020
Available online 28 September 2020

Keywords:
Hydrogen embrittlement
complex alloys
H absorption
surface energy

ABSTRACT

Hydrogen (H) embrittlement in multicomponent austenitic alloys is a serious limitation to their application in many environments. Recent experiments show that the High-Entropy Alloy (HEA) CoCrFeMnNi absorbs more H than 304 Stainless Steel but is less prone to embrittlement while the HEA CoCrFeNi is not embrittled under comparable conditions. As a first step toward understanding H embrittlement, here a comprehensive first-principles study of H absorption, surface, and fracture energies in the presence of H is presented for 304 Stainless Steel, 316 Stainless Steel, CoCrFeNi, and CoCrFeMnNi. A collinear paramagnetic model of the magnetic state is used, which is likely more realistic than previous proposed magnetic states. All alloys have a statistical distribution of H absorption sites. Hence, at low concentrations, H is effectively trapped in the lattice making it more difficult for H to segregate to defects or interfaces. Agreement with experimental H solubilities across a range of chemical potentials can be achieved with minor fitting of the average H absorption energy. The (111) surface energies for 0, 50, and 100% H surface coverage are very similar across all alloys. The fracture energies for two representative thermodynamic conditions are then determined. SS304 and CoCrFeNi are found to have the lowest fracture energies, but experiments suggest rather different embrittlement tendencies. These results indicate that differences in H embrittlement across these austenitic alloys are not due solely to differences in H absorption or H-reduced fracture energy, thus requiring more sophisticated concepts than those recently found successful for fcc Ni.

1. Introduction

As society moves toward a carbon-free economy, the importance of clean hydrogen (H) is rapidly growing. Unfortunately, H embrittles many metals reducing toughness and ductility at very low H concentrations, and so undermining the development of engineering components exposed to H [1–3]. There is thus now an urgent need to understand the mechanisms of H embrittlement (HE) and, moreover, to develop new metals that are immune to this dangerous degradation process. Currently, no consensus exists on the physical mechanisms of this long-standing problem, inhibiting the discovery of new alloys resistant to HE. However, the new class of High Entropy Alloys (HEAs), which are essentially random crystalline alloys composed of many elemental components all at high concentrations, have emerged and show promise [4–6]. Some face-centered cubic (fcc) HEAs in the Co-Cr-Fe-Mn-Ni family have impressive high yield strengths, ductility, and/or fracture toughness [7,8]. More importantly, several HEAs have now been shown to be more resistant to H embrittlement than Ni and 304 stainless steel ($Cr_{0.19}Fe_{0.74}Ni_{0.07}$; hereafter SS304). In particular, Zhao et al. showed that CoCrFeMnNi absorbs only slightly more H than SS304 under the same charging conditions but is more resistance to HE [9]. Luo et al. even found that H in CoCrFeMnNi can be beneficial effect for strength and ductility [10]. Nygren et al. did report HE in both CoCrFeMnNi and SS304 charged at higher gas pressure and tested at a much slower strain rate [11]. But under the same charging conditions, Nygren et al. did not observe HE in 316L stainless steel ($Cr_{0.18}Fe_{0.7}Ni_{0.12}$; hereafter SS316L) [12]. They then studied CoCrFeNi and found that it absorbs more H than Ni but shows no signs of HE [13]. Furthermore, Bertsch et al. found severe HE in Ni under the same charging conditions as Nygren [14]. The ordering of susceptibility to HE is thus Ni ~ SS304 > CoCrFeMnNi > SS316L ~ CoCrFeNi. Increasing HE is usually connected to increasing H concentration in the lattice, with many mitigation strategies aimed at creating H traps. The HEAs thus present an un-

* Corresponding author.
E-mail address: x.zhou@epfl.ch (X. Zhou).

https://doi.org/10.1016/j.actamat.2020.09.070
1359-6454/

resolved but promising paradox: they absorb more H than Ni and SS304 but are more resistant to embrittlement.

Despite intensive study over more than a century, there is little consensus on the underlying mechanisms of embrittlement. It is established that H will segregate to dislocations, grain boundaries, and interfaces [15–19], and that embrittlement increases with increasing H content. It is also established that H can lower surface energies and hence fracture energies in elemental metals [20,21], and this drives materials toward the possibility of embrittlement. The Hydrogen-Enhanced Decohesion (HEDE) model is based on the reduction of surface energy due to H, and recent work has shown one mechanistic pathway by which embrittlement can occur in Ni [22], which is the prototypical fcc metal for studying H embrittlement [23,24]. The Hydrogen-Enhanced Localized Plasticity model (HELP) envisions that H atoms influence either dislocation motion or interactions, leading to localized fracture [25,26]. Observations of nanoscale voids in H-containing alloys suggests yet other possibilities [27]. Yet another model envisions that H at a crack tip blocks dislocation emission, and thus promotes crack cleavage and prevention of ductile failure models [28,29]. A recent model suggests that H enhances decohesion sufficiently to enable a crack to accelerate up to speeds at which plasticity is reduced, leading to brittle fracture [30]. In most of these mechanistic concepts, it is important to understand H absorption into the lattice, H segregation to defects, H transport to cracks, and H effects at crack tips and surfaces.

In light of the above, we embark here on a study of the effects of H across a class of austenitic stainless steels including the High Entropy Alloys, seeking differences in behavior that may point toward mechanisms to explain the varying propensity for embrittlement across these alloys. We study two properties in these alloys, H absorption in the bulk and H absorption at the (lowest energy) (111) surfaces, using first-principles density functional theory. The use of first principles calculations to study fracture energy in pure metals and dilute alloys and at grain boundaries is fairly common (see, for instance, Hayes et al. [31] studied the ideal fracture energy in absence of impurities for pure metal system by first-principles calculations. Yamaguchi et al. [32] investigated grain boundary decohesion by sulfur in Fe and Ni. Hajilou et al. [33] studied the effect of co-segregation of H and sulfur on Ni grain boundary decohesion). However, there is limited work on less-dilute alloys and/or the effects of H on the fracture energy. Early works on effects of H include Jiang et al. [20] in Ni and Fe and Van der Ven et al. [34] in Al. No systematic study has examined the influence of H in complex alloys.

Here, we first show that a paramagnetic model gives T=0K total energies that are only a few meV/atom larger than the magnetic states studied previously for these paramagnetic alloys. We thus use this paramagnetic state for further studies on these paramagnetic alloys. We then find, not surprisingly, that there is a distribution of H absorption sites in a multicomponent alloy, which motivates modeling along the lines of those developed decades ago for H in amorphous metals [35]. We further find that, while H reduces the (111) surface energies of all alloys significantly, there are no significant differences among alloys. Combining bulk and surface absorption, we compute the room-temperature fracture free energy for the (111) surfaces using a simple solution model. At 100% H coverage, SS304 has the lowest fracture energy, but the fracture energy of CoCrFeNi is lower than those of SS316L and CoCrFeMnNi even though CoCrFeNi is the least susceptible to embrittlement. All together, our results indicate that at low H concentration (~ 1000 appm), H is trapped in the lower-energy tail of the distribution of absorption sites. The austenitic alloys should then in general be less susceptible to embrittlement than Ni due to (effectively) trapping in the bulk that reduces segregation to grain boundaries, interfaces, or dislocations, and thus retarding embrittlement mechanisms related to these phenomena. But the differences among the alloys in both absorption and fracture free energy are small, and cannot be related to experimentally-observed differences in their embrittlement. These findings thus point to the need to study other phenomena and mechanisms for embrittlement, such as that proposed by Song et al. [36].

The reminder of present paper is organized as follows. Section 2 introduces the computational methodology and a careful assessment of different possible magnetic states for all alloys considered. Section 3 then presents results for the H absorption in the paramagnetic alloys, and comparisons of the predicted absorption versus experiments. Section 4 examines the (111) surface energies with varying amounts of absorbed H, and then the fracture free energies. In Section 5, we discuss our findings further and draw some conclusions regarding effects of H in these austenitic alloys.

2. Computational methodology and bulk H-free alloys

First-principles DFT calculations are performed using the Vienna ab initio Simulation Package (VASP) within the generalized gradient approximation (GGA) and with the Perdew-Burke-Ernzerhof (PBE) functional [37–39]. The projector augmented wave (PAW) method [40] is used for handling core electrons, with valence electron configurations Co:$3d^8 4s^1$, Cr:$3d^5 4s^1$, Fe:$3d^7 4s^1$, Mn:$3d^6 4s^1$, and Ni:$3d^9 4s^1$. Collinear spin polarization is used in for all calculations. A plane-wave cut-off energy of 450 eV, a first-order Methfessel-Paxton smearing method with smearing parameter 0.1 eV, and a gamma-centered k-mesh with spacing 0.02 $Å^{-1}$, are also used for all calculations [41,42]. The convergence criterion for electron energy relaxation and ionic force relaxation are 10^{-6} eV and 10 meV/Å, respectively.

The chemical and magnetic disorder of the complex alloys are emulated using special quasi-random structures (SQS) generated by the ATAT code [43,44]. For studies of H in the bulk crystal, we use SQS structures with 120 atoms in a supercell of dimensions $2 \times 3 \times 5$ in terms of the fcc cubic unit cell. For studies of H on the (111) surfaces of the alloys, we use an SQS structure containing 9 (111) planes (180 atoms total) with orthogonal axes [$\bar{1}\bar{1}2$], [110] and [111]. A 12 Åvacuum distance is used between the two surfaces in the periodic cell to minimize any surface interactions. Each SQS surface is random, and thus may deviate slightly from the precise composition, leading to an uncertainty in the surface energies. However, a study on CoCrFeMnNi using four different SQS containing 96 atoms (16 surface atoms) shows sample-to-sample variations of only ~ 1.5% and so the results quoted below on the larger-area samples are expected to be accurate.

It is well-established that the magnetic structures of these types of alloys are of critical importance in understanding their physical properties. Alloys having a combination of ferromagnetic (FM) Co, Fe, and Ni and anti-ferromagnetic (AFM) Cr and Mn lead to a range of possible theoretical magnetic states. The real alloys are all paramagnetic (PM) at low temperatures, but accurate modeling of a realistic PM state is computationally not feasible for the scope of studies needed here [45,46]. With the aim of studying both bulk and surface structures in a paramagnetic state, we have first examined the total energies of several representative magnetic states for each alloy.

Specifically, we consider several initial magnetic states. One state is the AFM state in which the initial spin arrangement alternates in sign layer by layer in the [001] direction. A second state is the PM state in which the initial spins of $\pm 3\mu_B$ for Co, Cr, Mn, and Fe, and $\pm 1\mu_B$ for Ni are randomly distributed. A third state for SS304 and SS316L is a magnetic state in which Fe and Ni are spin-up and Cr is spin-down, denoted here as Fe↑Cr↓Ni↑, which was previously proposed as possible state for stainless steel [47]. A third state for CoCrFeNi is a taken to have Fe, Ni, and

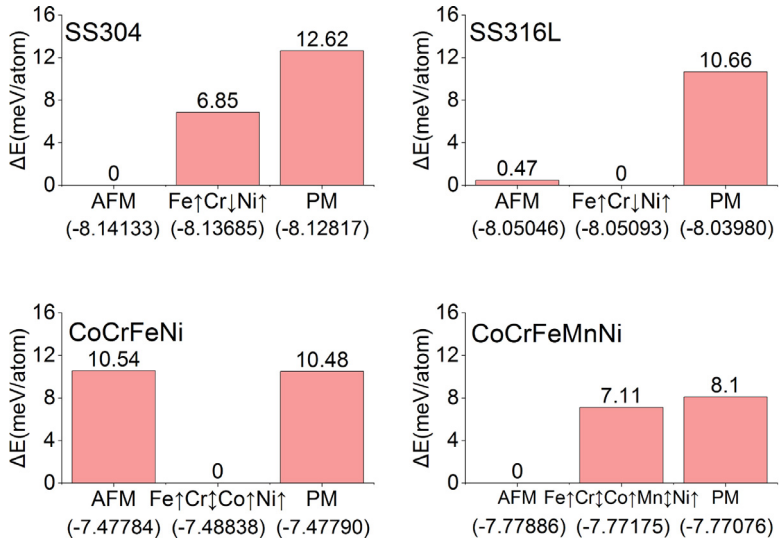

Fig. 1. Energy difference between each magnetic state and the lowest energy magnetic state for the SSs and HEAs. The value in parentheses is the total energy per atom for each case.

Co spin up and Cr equally spin up and spin down, denoted as Co↑Cr↕Fe↑Ni↑ and examined previously by Niu et al. [48]. A third state for CoCrFeMnNi is similar, with the Mn equally spin up and spin down, denoted as Co↑Cr↕Fe↑Mn↕Ni↑ and examined previously by both Schneeweiss et al. [49] and Niu et al. [50]. After full electronic and ionic relaxations, we find the total energies per atom of all three magnetic states to be very close for all alloys, as shown in Fig. 1. For SS304, the AFM state has the lowest energy but the Fe↑Cr↓Ni↑ state is only 0.00685 eV/atom higher, and the PM state only 0.01262 eV/atom higher in energy. For SS316L, the Fe↑Cr↓Ni↑ and AFM state differ by only 0.00047 eV/atom, while the PM state is higher in energy by only 0.01066 eV/atom. CoCrFeNi shows the Co↑Cr↕Fe↑Ni↑ to be lowest in energy by about 0.01 eV/atom relative to both the AFM and PM states, which are almost identical in energy. CoCrFeMnNi has AFM as the lowest energy state, with Co↑Cr↕Fe↑Mn↕Ni↑ only 0.00711 eV/atom higher and the PM state just slightly less favorable at 0.0081 eV/atom higher. From these results, we conclude that there is no single consistent lowest-energy magnetic configuration across all alloys. Moreover, we find that the PM state, while never the lowest energy state, is typically close (~ 10 meV/atom) to the lowest energy state.

Examining the relaxed magnetic states, Fig. 2 shows that the distribution of magnetic moments on each type of atom are very similar between the AFM and PM states in all alloys, both differing significantly from the more-polarized third configuration. However, the spatial distribution of spins in the AFM and PM structures remain different, with the AFM preserving a layered structure and the PM remaining more disordered (see Fig. 3). There is some tendency toward local AFM-type planar ordering in some planes of the PM state, mainly for SS304 and SS316L. Thus, the relaxed PM state does tend toward the AFM state to some degree but remains distinct. At finite temperatures, and in particular room temperature where we are interested in studying H in the alloys, there is an entropic contribution that should lower the free energy of the PM state relative to the more-ordered states. Since these alloys are paramagnetic at low temperatures, we proceed with an analysis of the energetics of H in these alloys and their surfaces using the PM structure only.

3. H absorption in bulk austenitic alloys

H absorption into interstitial sites in the crystalline lattice provides the baseline energetics from which subsequent segregation to defects and surfaces is assessed. Here, we introduce H into 50 chemically and magnetically different environments in each of the four alloys studied here, using the initial PM state examined in the previous section. For each individual interstitial site, the H absorption energy E_{ab} is defined relative to the energy of H in the H_2 molecule as

$$E_{ab} = E_{tot}[mM + nH] - E_{tot}[mM] - \frac{1}{2}E_{tot}[H_2] \quad (1)$$

where $E_{tot}[mM]$ is the total energy of a particular random realization of a given alloy having m metal atoms in the supercell, $E_{tot}[mM + nH]$ is the energy of the same system with one H atom in one octahedral interstitial site of the alloy, and $E_{tot}[H_2]$ is the total energy of H_2 molecule. In elemental fcc metals, the octahedral interstitial site has a lower energy than the tetrahedral site and limited tests find similar results for the fcc alloys, so our results here focus exclusively on the octahedral sites.

Fig. 4 shows the spectrum of H absorption energies computed for H introduced into 50 different octahedral sites in each alloy. In general, there is a distribution of absorption energies in each alloy corresponding to different local chemical and/or magnetic environments around the octahedral site occupied by H. The distribution for each alloy is well-represented by a Gaussian distribution with average energy and standard deviation denoted by $\bar{E}$ and σ, respectively, and shown in Fig. 4 and Table 1. The average absorption energy does not follow any clear trend with alloy complexity or composition. The standard deviation for the most-dilute (non-Fe solutes) alloy, SS304, is the lowest by a small margin but the other alloys do not follow any consistent trend with increasing solute concentrations relative to pure Fe.

We have examined whether any correlations exist between the H absorption energy and the chemical identities of the six first-neighbor metal atoms, and find no significant correlations. We have also examined whether any correlations exist between the H absorption energy and the net magnetic moment of the six first-neighbor (1NN) metal atoms, and again find no significant correlation. Finally, we have studied whether H alters the local magnetic moments of any of the surrounding metal atoms. As shown in Fig. 5, we find very limited changes, although there are occasional spin flips on individual atoms. The H absorption energies in the cases with such spin flips are not notably different than the energies in cases with small ($\Delta\mu$ ~ $\pm 0.2\mu_B$) changes in magnetic moments. This also indicates that the PM state is generally stable against the introduction of H.

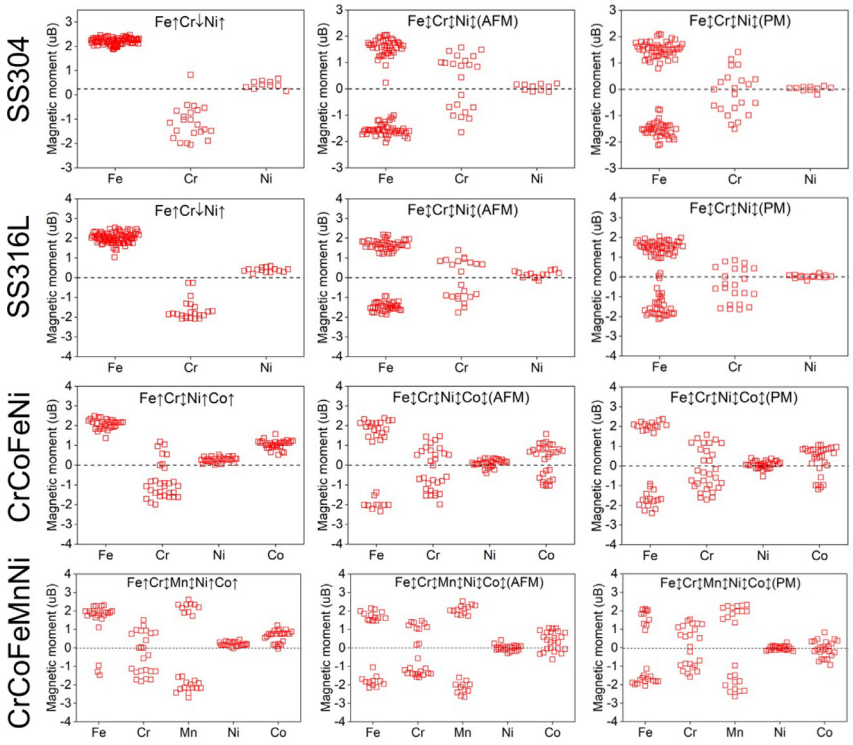

Fig. 2. Distributions of relaxed atomic magnetic moments arranged by atom type, for all four complex alloys with the various initial magnetic states studied here.

For completeness, we also investigated the H absorption energies for these alloys in the high ferromagnetic states that have been commonly used for studying other physical properties in complex alloys [48,50]. The results are shown in Appendix A, and show definite differences in the mean H absorption energies as compared to the PM state but rather similar standard deviations. Since the PM state is the most-relevant case for real alloys, we do not address other magnetic states further.

The statistical distribution of H absorption energies has implications for H-related phenomena in the alloys that will be discussed in Section 5. For now, we discuss how the distribution of H binding sites in an alloy impacts the H absorption, using the framework originally developed for H absorption in amorphous alloys. We first examine the H absorption as a function of temperature T and H chemical potential μ, and compare results obtained using the DFT energies to experimental data. The H binding distribution is actually a density of states $n(E_{ab})$, and we use a Gaussian distribution

$$n(E_{ab}) = \frac{1}{\sigma\sqrt{\pi}} exp\left[-\left(\frac{E_{ab}-\bar{E}}{\sigma}\right)^2\right] \quad (2)$$

The H solubility C_b in the bulk alloy can then be computed as

$$C_b = \int_{-\infty}^{+\infty} \frac{n(E_{ab})dE_{ab}}{1+exp\left(\frac{E_{ab}+E_{ZP}-\mu}{kT}\right)} \quad (3)$$

where k is Boltzmann's constant and E_{ZP} is the H zero-point energy in the alloy.

The E_{ZP} is computed as $E_{ZP} = \frac{\sum_{i=1}^{3} h\nu_i}{2}$ where the H vibrational frequencies $\{\nu_i\}$ are computed in DFT using the harmonic approximation with the metal atoms fixed at the relaxed positions. Each local H site in an alloy has, in principle, its own set of vibration frequencies. However, we have calculated these frequencies for a number of representative sites in each alloy. We find no correlation between the vibration frequencies and the local absorption energy E_{ab}. The distribution of frequencies leads to a distribution of E_{ZP} values, but the variations in E_{ZP} are significantly smaller than those for E_{ab}. We thus use the average values for each alloy [0.180 eV (SS304), 0.182 eV (SS316L), 0.176 eV (CoCrFeNi), 0.183 eV (CoCrFeMnNi)]. While the E_{ZP} itself is large, the differences among alloys are fairly small and, notably, rather smaller than the differences in $\bar{E}$ between the different alloys.

Table 1
DFT-computed mean absorption energy $\bar{E}$, shifted value needed to match experimental H absorption, and difference $\triangle\bar{E}$ between the shifted and DFT. All energies are in eV.

	SS304	SS316L	CoCrFeNi	CoCrFeMnNi
Computed $\bar{E}$	0.077	0.008	0.066	-0.016
Shifted $\bar{E}$	0.042	0.047	0.078	0.036
$\triangle\bar{E}$	-0.035	+0.039	+0.012	+0.052

The H chemical potential μ in the gas phase at temperature T and pressure P is well-established as

$$\mu = \frac{1}{2}\mu_{H_2}^{gas} = \frac{-1}{2kT} ln\left[\frac{kT}{P} \times \left(\frac{2\pi m_{H_2} kT}{h^2}\right)^2 \times \frac{exp(-h\nu_{H_2}/2kT)}{1-exp(-h\nu_{H_2}/2kT)} \times \frac{4\pi I_{H_2} kT}{h^2}\right] \quad (4)$$

where m_{H_2} is the mass of H_2 molecule, h is is Planck constant, ν_{H_2} is the vibrational frequency of the H_2 molecule, and I_{H_2} is the H_2 rotational moment of inertia.

We first evaluate the solubility of H in pure fcc Ni. In an elemental metal, the density of states is a delta function (σ=0), and DFT yields $\bar{E}$=0.09 eV with a E_{ZP}=0.149 eV for H in the Ni octahedral site. The predicted solubility of H in Ni as a function of chemical potential at various charging temperatures is shown in Fig. 6. The predictions agree very well with experimental solubilities with no adjustable parameters [11,23,51]. If we execute the same computations using the DFT results for the Fe-based austenitic alloys, we do not achieve agreement with experiments. The discrepancy could reside in $\bar{E}$, σ, or E_{ZP}. The standard deviation arises from

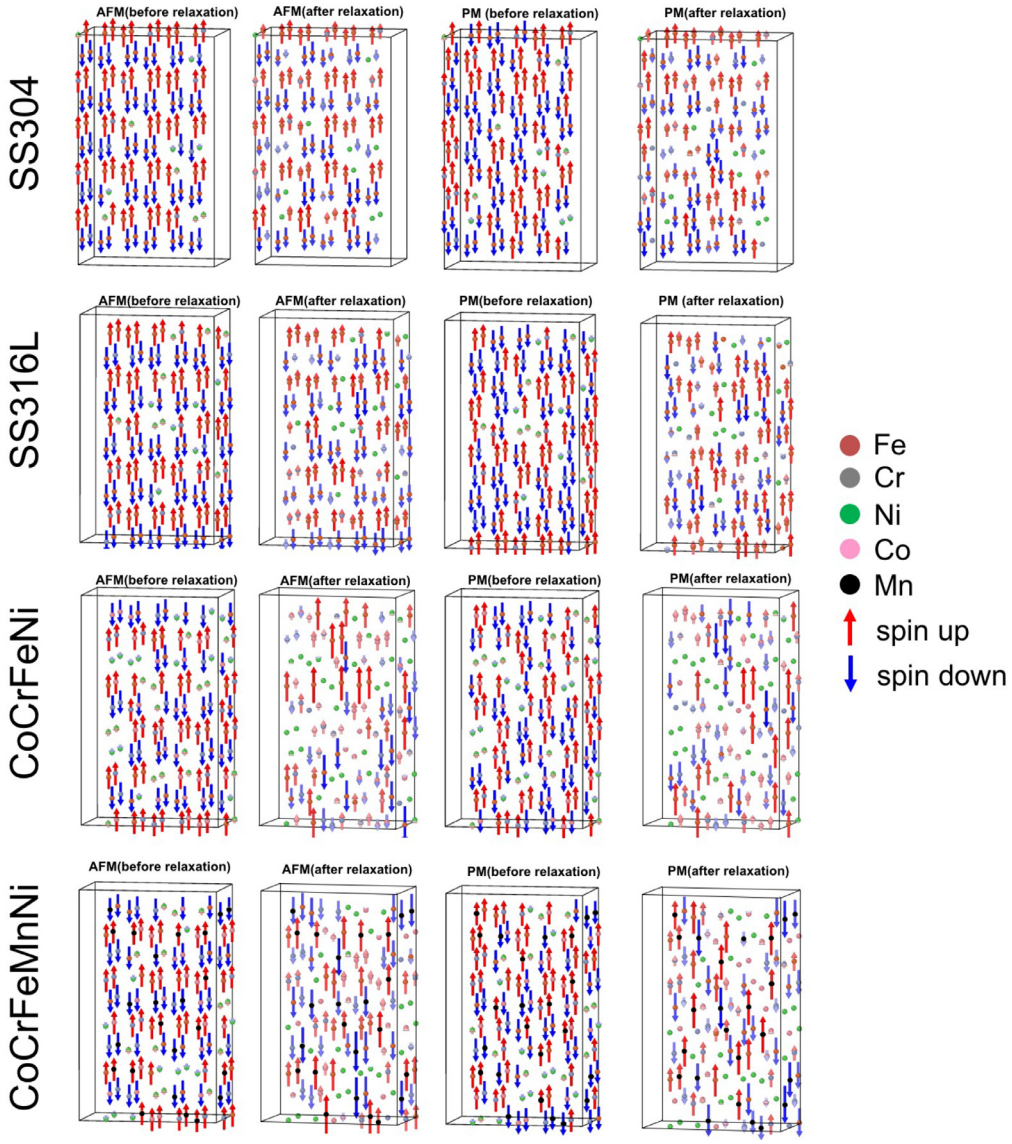

Fig. 3. Atom-by-atom distribution of magnetic moments before and after relaxation in the AFM and PM states, respectively.

computations on one random alloy differing only in the position of the one H atom. So, we assume that the differences in H energies within the same random sample are more realistic than the mean energy. We recall also that the standard deviations computed for the ferromagnetic states are also quite similar while the mean values differ from the PM state. We thus hold the standard deviation fixed and shift the mean $\bar{E}$ to fit the available experiments on each alloy; note that this shift could also be assigned to the E_{ZP}. Fig. 6 shows the computed concentrations versus H chemical potential across a range of temperatures for all four alloys, achieved using the shifted (fitted) values of $\bar{E}$ shown in Table 1. With one parameter for each alloy moderately shifted relative to the computed DFT value, we are able to capture many experiments in both SS304 and SS316L [9,11,52–57]. The more-limited experimental data on the CoCrFeMnNi is also well captured [9,11,58], while there is only one experimental measurement for CoCrFeNi [13].

Our analysis above assumes that the H-charged samples are in equilibrium. For gas-phase charging at elevated temperatures, the H diffusion rates should be sufficient for equilibrium to be achieved. Non-equilibrium distributions may be inferred from fracture tests revealing brittle domains near the sample surfaces and ductile domains in the interior, but this is perhaps more typical of electrochemical charging and the alloys examined here do not show mixed fracture surface morphologies. Finally, if different samples of the same alloy were not in equilibrium, an equilibrium analysis could not capture the measured H absorption across such a range of charging conditions, as shown in Fig. 6. These points support our assumption that the H-charged alloys studied here are in equilibrium.

4. Surface and fracture free energies of austenitic alloys in the presence of H

Many theoretical studies on elemental metals show that H atoms reduce the surface energy. This reduction of surface energy is widely assumed to assist in driving Hydrogen embrittlement, although the precise processes/mechanisms of embrittlement are not always identified. Here, we examine the trends in surface energy and fracture free energy versus H across the four austenitic alloys studied here to determine if there are any trends that correlate with the varying propensity for H embrittlement across these alloys.

We consider the low-energy (111) surface typically evaluated in fcc crystals, and we use the PM state for all alloys. We employ

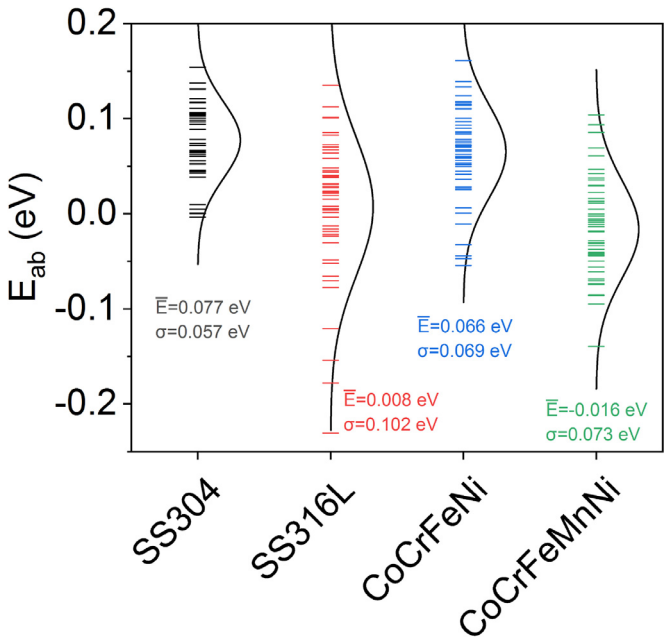

Fig. 4. DFT-calculated distribution of H absorption energies in the four random austenitic alloys having the PM structure, relative to H in H_2. The mean and standard deviation of each distribution is shown; there is no clear trend with either chemical composition or complexity.

the slab model with two free surfaces for which details were given in Section 2. For surfaces covered by H atoms, the surface energy $\gamma_s(H)$ is computed relative to the clean metal and H in H_2 gas at T=0 as

$$\gamma_s(H) = \frac{\left(E^S_{tot}[mM+nH]+nE^S_{ZP}[H]\right)-E^B_{tot}[mM]}{2A} - \frac{0.5n\left(E^{gas}_{tot}[H_2]+E^{gas}_{ZP}[H_2]\right)}{2A} \quad (5)$$

where $E^S_{tot}[mM+nH]$ is the total energy of the slab supercell with m metal atoms and n H atoms placed randomly in the H surface sites, $E^B_{tot}[mM]$ is the total energy of the bulk supercell containing m metal atoms and no H, $E^{gas}_{tot}[H_2]$ is the total energy of a single H_2 molecule, $E^S_{ZP}[H]$ and $E^{gas}_{ZP}[H_2]$ are the zero-point energies of H on the surface and H_2 molecule, respectively. We use the average E_{ZP} of H on the surface obtained from the DFT-computed H surface vibrational frequencies (0.174 eV (SS304), 0.172 eV (SS316L), 0.173 eV (CoCrFeNi), 0.178 eV (CoCrNiFeMnNi), respectively). The average E_{ZP} values of H on the surface are slightly lower than those in the bulk lattice, as expected, but again are quite similar across all four alloys. Note that Eq. 5 above includes the H-free surface ($n = 0$).

Table 2
DFT calculated (111) surface energies for H coverages C_s of 0, 50, and 100% in the PM state, for all four alloys (in J/m^2).

C_s	surface energy $\gamma_s(H)$			
	SS304	SS316L	CoCrFeNi	CoCrFeMnNi
0	2.41	2.32	2.23	2.26
0.5	1.53	1.34	1.35	1.36
1.0	0.63	0.60	0.56	0.57

Table 2 shows the calculated surface energies versus H concentration C_s in SS304, SS316L, CoCrFeNi and CoCrFeMnNi at 0%, 50% and 100% H coverage (i.e C_s=0, 0.5, 1.0). At 50% coverage, the sur-

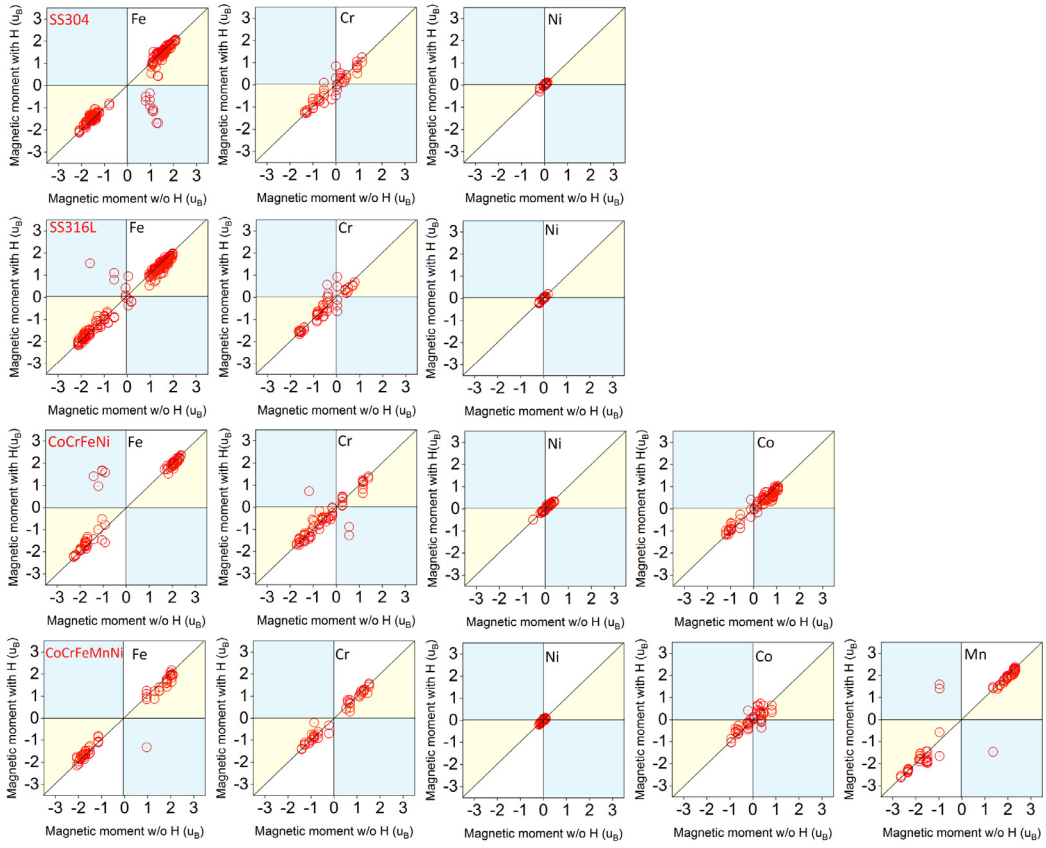

Fig. 5. Magnetic moments of the 6 near-neighbor metal atoms around an H atom after introduction of H versus their magnetic moments before introduction of the H atom. Results are divided according to the element type in each alloy. Points falling within the light yellow triangles indicate a decreased magnetic moment upon introduction of H. Points falling within the blue rectangular regions indicate magnetic moments that have changed sign upon the introduction of H.

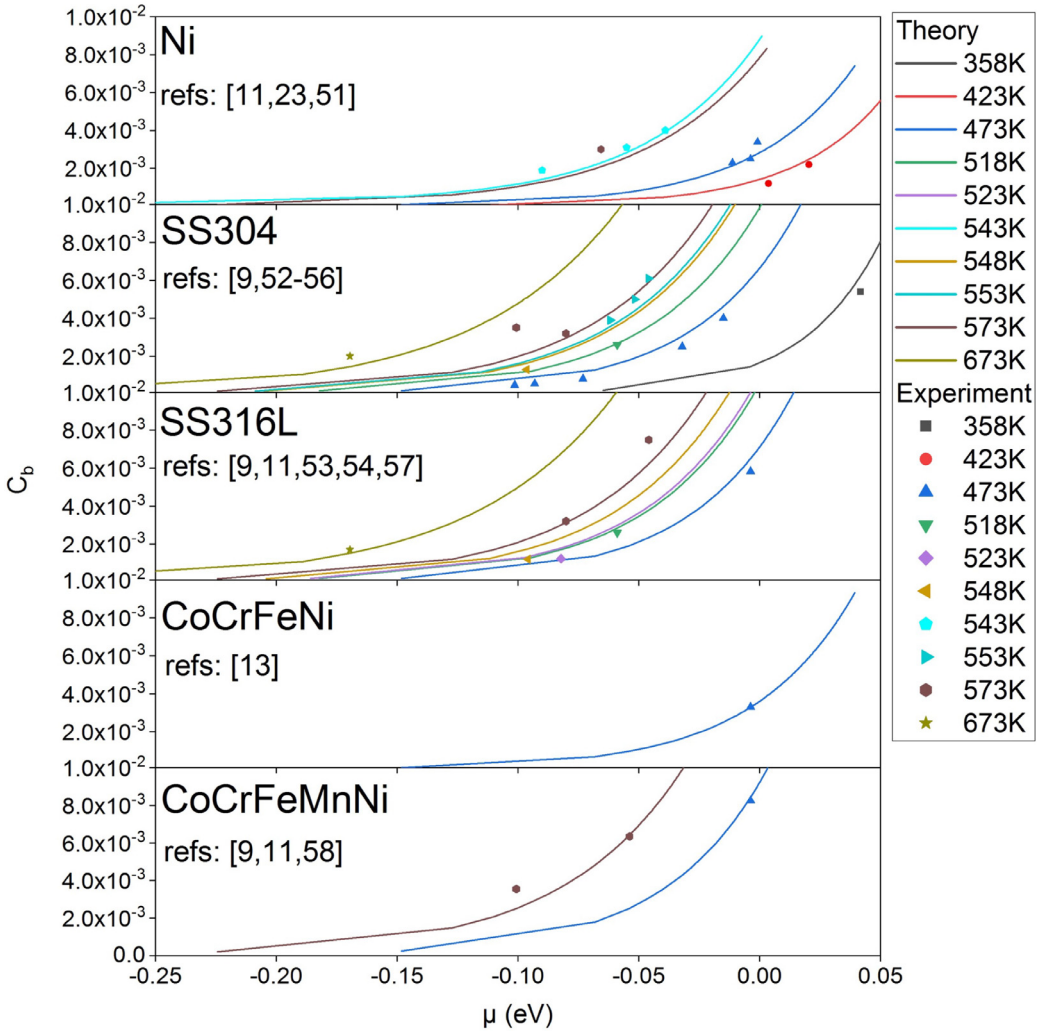

Fig. 6. Experimental and predicted H solubility vs. chemical potential in Ni and the four austenitic alloys studied here at various temperatures as indicated. For the alloys, the mean absorption energy $\bar{E}$ has been fitted to obtain the best match with experiments (see Table 1). Sources of experimental data are shown in each sub-figure.

face site occupation is random rather than a surface where the lowest energy sites are occupied; the latter would be computationally challenging to determine. The H-free surface energies are quite close, with the HEAs slightly lower (0.06-0.09 J/m^2) than SS316L which is, in turn, 0.1 J/m^2 lower than SS304. Rak et al. studied the (111) surface energies of SS304 and SS316L using SQS supercells with an initial FM state and obtained very similar values (2.25 J/m^2 for SS304 and 2.32 J/m^2 for SS316L) [47].

More importantly, the presence of H on the surfaces of all these alloys reduces the surface energies steadily with increasing H coverage. At full 100% H coverage, the surface energies are reduced by 74.4 ± 0.5% for all four alloys. While this is a dramatic reduction of surface energy due to H, there is almost no variation among the alloys. Thus, the observed differences in Hydrogen embrittlement across these alloys cannot be related to the reductions in (111) surface energy due to H. The surface energy relative to H_2 gas is not, however, the same as the fracture free energy, and so additional considerations are needed as discussed next.

The fracture free energy γ_F is the difference in free energy between a bulk material with H at concentration C_b and a surface of the material with H surface concentration C_s (and concentration C_b remaining in the infinite bulk). The major contributions to the free energy are the H-free surface energy, the additional change in surface energy due to the presence of H, and the changes in energy, E_{ZP}, and entropy of H atoms in moving from the dilute bulk ($C_b << 1$) to the concentrated surface ($C_s \sim 1$). We neglect other contributions to the free energy include those due to vibrational and magnetic effects. The energetic contribution γ_F^{En} to the surface free energy is

$$\gamma_F^{En}(H) = \frac{\left(E_{tot}^S[mM+nH]+nE_{ZP}^S[H]\right)-E_{tot}^B[mM]}{2A} - \frac{n\left(E_{tot}^B[mM+1H]-E_{tot}^B[mM]+E_{ZP}^B[H]\right)}{2A} \quad (6)$$

Comparing Eqs. 5 and 6, the difference is in the reference energy. The fracture free energy is relative to H in the bulk rather than the arbitrary reference of H_2 gas. The bulk H absorption energies are statistically-distributed, and occupation of sites is determined by the thermodynamic conditions. So, the "bulk reference" above must be taken as the average absorption energy of the occupied states in the bulk. The average is appropriate because the distribution of H in the bulk after segregation of an infinitesimal fraction of H to the surface is unchanged, and so effectively H is taken from individual absorption energies in proportion to their occupation in the bulk. We note that the correct occupation is that used at the application or testing temperature (e.g. 300K) and not the temperature at which the H charging was executed. Thus, the distribution of H is that corresponding to the current temperature T and the H concentration C_b after charging; unlike during charging,

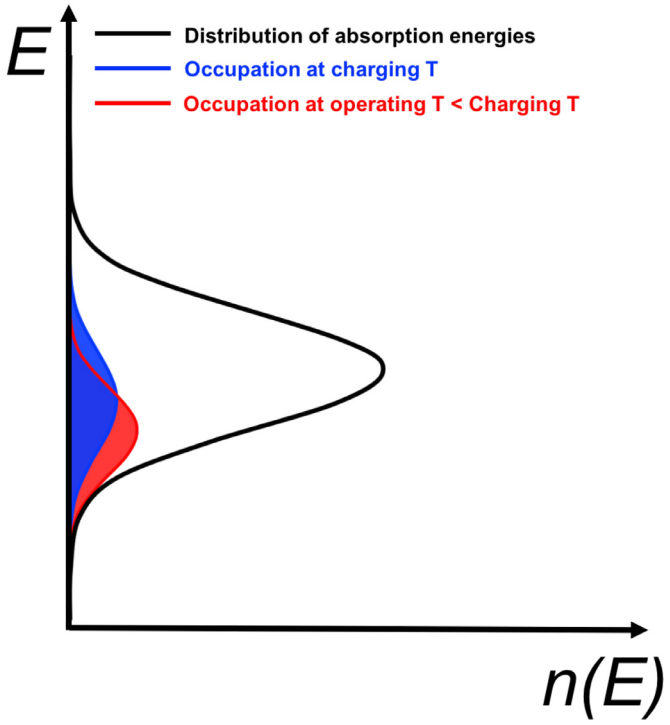

Fig. 7. Schematic illustration of distribution of absorption energies.

the chemical potential is not specified but is instead an outcome of the redistribution. Fig. 7 shows a schematic of the total distribution of H absorption sites in the bulk, the occupied sites under the charging conditions (fixed T and P, and hence fixed μ), and the occupation of sites under application conditions (fixed lower T and fixed C_b). Since the application temperature is typically lower than the charging temperature, the average H occupation energy is also lower.

We recall that to match the experimentally-measured H concentrations in the various alloys charged under varying conditions required a fitted shift in the average absorption energy for each alloy. However, in computing fracture energies that involve the difference between H energies in the bulk and H energies on the surface, we use only DFT data with *no shift* in the bulk energies. There is no basis for making any shift/fit to the surface energies, and a difference between two DFT computations in nominally the same alloy system studied in the same manner is the most robust approach.

The entropy contribution to the fracture free energy γ_F^{Ent} is obtained using a simple solution model. A full calculation using the distribution of occupied states in the bulk alloy leads to the deceptively simple result

$$\gamma_F^{Ent}(H) = \frac{-kT}{A_0}[-(1-C_S)ln(1-C_S) - C_S lnC_S + C_S lnC_b] \quad (7)$$

where C_S is H coverage on the surface, C_b is bulk concentration, k is Boltzmann constant and A_0 is the area per (111) surface site. This result is the same as obtained in an elemental metal (unique site energy) [22], so the existence of a distribution of sites is not important for determining the total entropic contribution.

From the above, we see that the fracture free energy is a function of the charging conditions due to its dependence on the occupation of H sites in the bulk. We examine the fracture free energy for two representative experimental charging conditions used by Zhao et al. and Nygren et al. Fig. 8 shows the calculated fracture free energies versus H at 300K. At 100% coverage, the entropic contribution is on the order of 0.4 J/m^2, representing a non-negligible contribution to the fracture free energy. Entropy thus makes fracture less favorable than suggested by the surface energy alone

Comparing different alloys, for charging under the Zhao conditions, SS304 at 100% H coverage has the largest reduction in fracture free energy (61%) and the lowest absolute value. The CoCrNiFe alloy has the second-lowest value, followed by SS316L and CoCrFeMnNi, respectively. Under the more-aggressive Nygren charging conditions, the fracture free energy is again the lowest for SS304 and the largest for CoCrFeMnNi, but the SS316L becomes slightly lower than CoCrNiFe. In spite of higher bulk H concentrations for the Nygren charging conditions, the surface free energy reductions are not significantly larger than those for the Zhao et al. charging conditions. This is a consequence of both the lower entropy con-

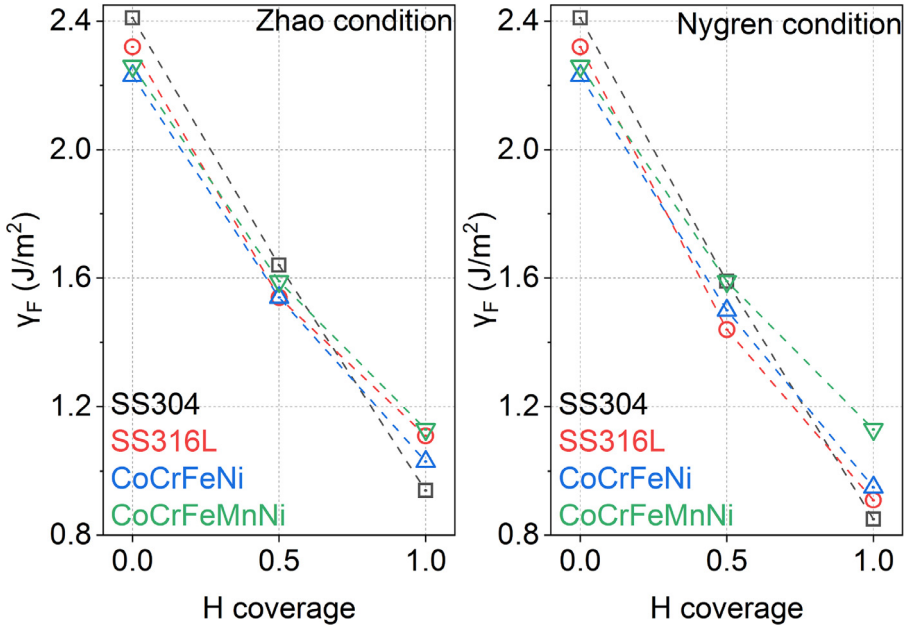

Fig. 8. Fracture free energy at 300K after charging under Zhao (P=15MPa, T=573K) [9] and Nygren (P=120MPa, T=473K) [11] conditions for the four alloys studied here.

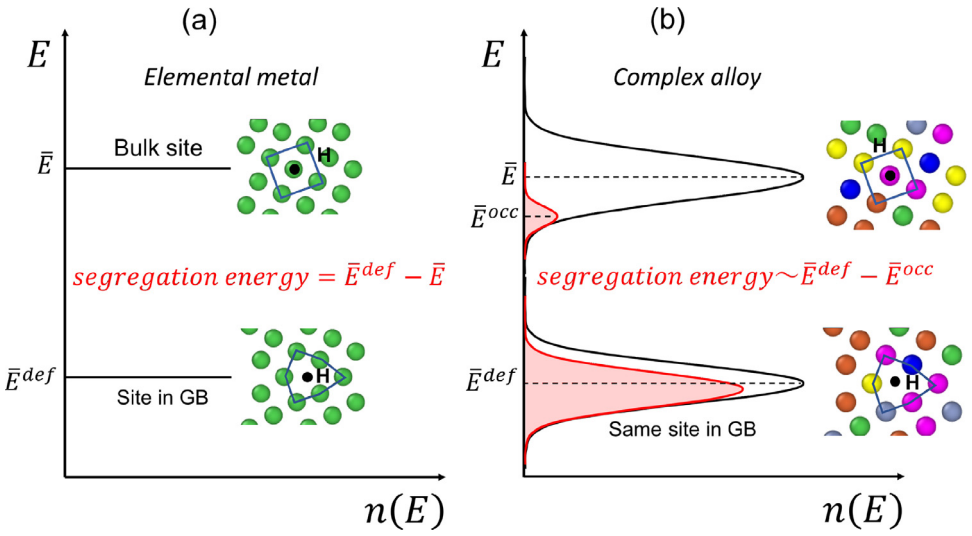

Fig. 9. Schematic illustration of distribution of absorption energies.

tribution for the Nygren conditions and the higher average absorption energy for occupied H in the bulk alloy.

The fracture free energy results would imply that the susceptibility to H embrittlement is highest in SS304 and lowest in the Cantor alloy, with SS316L and CoCrFeNi being intermediate and close. Experimental observations show the relative H susceptibility to be SS304 > CoCrFeMnNi > SS316L ~ CoCrFeNi. While our results are consistent with SS304 being most susceptible, the overall ordering based on the fracture free energies differs from experiments. In addition, the differences in fracture energy among the alloys are quite small. Therefore, embrittlement cannot be determined solely by the reduction of fracture free energy caused by H, as determined by the computational results obtained here.

5. Discussion and summary

The existence of a distribution of H binding energies has general implications for the segregation of H to defects. The lower tail of the distribution $E_{ab} << \bar{E}$ represent strong binding sites for H. The H concentrations typically generated by charging at high external H_2 pressure and moderately high temperature are low, $C_b << 1$, and so the states actually occupied by H reside predominantly in the low-energy tail of the energy distributions (see Fig. 7). The precise distribution of occupied states under any conditions can be computed using Eq. 3. Embrittlement mechanisms usually involve the segregation of H to a defect (grain boundary, dislocation, interface with an inclusion, crack tip) at significantly higher concentrations $C_d \sim 1$ because the binding energy at the defect is negative relative to the bulk. For an elemental metal, the bulk absorption energy is a single value $\bar{E}$ and the defect has a set of distinct sites, each of which a particular binding energy; one site in a grain boundary is indicated in Fig. 9a with defect energy $\bar{E}^{def}$. The segregation energy at the defect site is then $\bar{E}^{def} - \bar{E}$. In the complex alloy, the sites occupied by H in the bulk lie in the lower tail of the distribution with an average $\bar{E}^{occ} < \bar{E}$, as indicated in Fig. 9b. The same geometrical H site at the defect also has energies that are statistically distributed around $\bar{E}^{def}$. However, the H occupation of this site is higher, and so the typical difference in segregation energy is approaching $\bar{E}^{def} - \bar{E}^{occ}$, which is smaller than in the elemental metal. The segregation of H to defects is thus energetically more costly in the random alloy as compared to an equivalent homogeneous alloy having the same $\bar{E}$.

The situation above could be complicated by explicit segregation of alloy elements to a defect. However, such segregation phenomena are not relevant for defects that evolve with deformation (e.g. dislocations and crack tips). Furthermore, segregation would only arise for static defects (grain boundaries and inclusion interfaces) given sufficient time at elevated temperatures during material processing and not during application conditions at room temperature.

The role of the distribution of bulk absorption energies is evident in our computation of the surface free energy. The energy difference between the low-energy occupied bulk H sites and the nearly-fully-occupied H sites on the surface is reduced, relative to that obtained using the average bulk absorption energy. The reduction in surface free energy due to H is thus not as large, and this inhibits any H-induced fracture phenomena.

We do not find significant quantitative differences among the four alloys studied here. The trends for H absorption cannot be captured by the direct DFT results, and the shifts necessary to match experiments, while small, are not systematic across the alloys. The fracture free energies are very similar across the four alloys. We do find that SS304 has the lowest fracture free energy, and so should be the most susceptible to embrittlement, consistent with experiments. However, among the other three higher-concentration alloys no clear trend emerges that is consistent with experiments. Hydrogen-enhanced decohesion mechanisms based only on reducing fracture free energy thus appear insufficient to explain the existing experiments, atleast as computed using DFT.

In summary, comprehensive first-principles calculations were performed to study the H absorption in 4 representative fcc alloys in the Co-Cr-Fe-Mn-Ni family (SS304, SS316L, CoCrFeNi and CoCrFeMnNi). A PM magnetic state was found to be slightly higher-energy than other proposed magnetic states, but is used as a more-realistic model for actual paramagnetic alloys. The absorption energies of H in the alloys show a statistical variation due to local differences in environment, and this has implications for H absorption and segregation to defects. Small shifts in the mean absorption energy are needed to match extensive experiments of H absorption versus temperature and H_2 gas pressure. These shifts may reflect the limits of DFT for quantitative predictions and, more importantly, deducing trends with alloy composition. The surface and fracture free energies of all alloys are strongly reduced in the presence of H, providing a strong driving force for brittle fracture, but the detailed trends do not follow subtle experimental differences. These differences may be beyond the reliability of the current DFT methods and treatment of magnetism, and hence comparisons of the present DFT results to more-advanced treatments should be

pursued. However, the influence of a statistical distribution of H absorption energies in bulk alloys is a robust conceptual result. Its effects, both qualitative and quantitative, on the operation of various proposed mechanisms for H embrittlement must be investigate in more detail.

Declaration of Competing Interest

The authors declare that they have no known competing financial interests or personal relationships that could have appeared to influence the work reported in this paper.

Acknowlgedgments

This work was supported by the Swiss National Science Foundation project “Harnessing atomic-scale randomness: design and optimization of mechanical performance in High Entropy Alloys”, project “200021_18198/1”. The authors also acknowledge support of high-performance computing provided by Scientific IT and Application Support (SCITAS) at EPFL.

Appendix A. H absorption energies in high ferromagnetic state

Fig. A.1 shows the calculated absorption energies of H in examined complex alloys in high ferromagnetic state. It is found the standard deviation is similar to that in the PM state. But the mean value is different, suggesting the magnetic state plays the important role in H absorption energies.

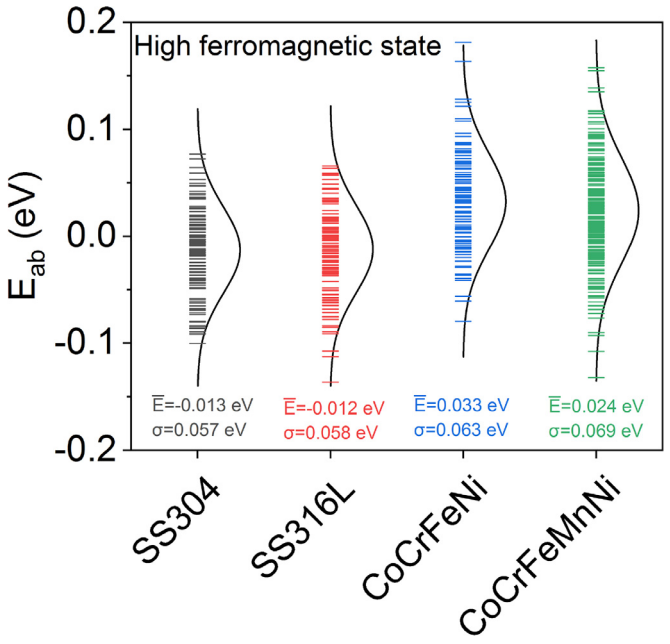

Fig. A.1. DFT-calculated distribution of H absorption energies in the four random austenitic alloys having the high ferromagnetic structure, relative to H in H_2.

References

[1] W.H. Johnson, On some remarkable changes produced in iron and steel by the action of hydrogen and acids, Proceedings of the Royal Society of London 23 (156-163) (1875) 168–179.
[2] M. Louthan, G. Caskey, J. Donovan, D. Rawl, Hydrogen embrittlement of metals, Materials Science and Engineering 10 (1972) 357–368.
[3] H. Johnson, Hydrogen embrittlement, Science 179 (4070) (1973) 228–230.
[4] Y. Zhang, T.T. Zuo, Z. Tang, M.C. Gao, K.A. Dahmen, P.K. Liaw, Z.P. Lu, Microstructures and properties of high-entropy alloys, Progress in Materials Science 61 (2014) 1–93.
[5] J. Yeh, S. Chen, S. Lin, J. Gan, T. Chin, T. Shun, C. Tsau, S. Chang, Nanostructured high-entropy alloys with multiple principal elements: novel alloy design concepts and outcomes, Advanced Engineering Materials 6 (5) (2004) 299–303.
[6] O. Senkov, G. Wilks, D. Miracle, C. Chuang, P. Liaw, Refractory high-entropy alloys, Intermetallics 18 (9) (2010) 1758–1765.
[7] B. Gludovatz, A. Hohenwarter, D. Catoor, E.H. Chang, E.P. George, R.O. Ritchie, A fracture-resistant high-entropy alloy for cryogenic applications, Science 345 (6201) (2014) 1153–1158.
[8] Y. Zhang, T.T. Zuo, Z. Tang, M.C. Gao, K.A. Dahmen, P.K. Liaw, Z.P. Lu, Microstructures and properties of high-entropy alloys, Progress in Materials Science 61 (2014) 1–93.
[9] Y. Zhao, D. Lee, M. Seok, J. Lee, M. Phaniraj, J. Suh, H. Ha, J. Kim, U. Ramamurty, J. Jang, Resistance of CoCrFeMnNi high-entropy alloy to gaseous hydrogen embrittlement, Scripta Materialia 135 (2017) 54–58.
[10] H. Luo, Z. Li, D. Raabe, Hydrogen enhances strength and ductility of an equiatomic high-entropy alloy, Scientific reports 7 (1) (2017) 1–7.
[11] K.E. Nygren, K. Bertsch, S. Wang, H. Bei, A. Nagao, I. Robertson, Hydrogen embrittlement in compositionally complex FeNiCoCrMn fcc solid solution alloy, Current Opinion in Solid State and Materials Science 22 (1) (2018) 1–7.
[12] K.E. Nygren, The influence of hydrogen on the evolving microstructure during fatigue crack growth in metastable and stable austenitic stainless steels, University of Illinois at Urbana-Champaign, 2016 Ph.D. thesis.
[13] K.E. Nygren, S. Wang, K.M. Bertsch, H. Bei, A. Nagao, I.M. Robertson, Hydrogen embrittlement of the equi-molar FeNiCoCr alloy, Acta Materialia 157 (2018) 218–227.
[14] K. Bertsch, S. Wang, A. Nagao, I. Robertson, Hydrogen-induced compatibility constraints across grain boundaries drive intergranular failure of Ni, Materials Science and Engineering: A 760 (2019) 58–67.
[15] R. Kirchheim, Reducing grain boundary, dislocation line and vacancy formation energies by solute segregation: II. experimental evidence and consequences, Acta Materialia 55 (15) (2007) 5139–5148.
[16] M. Ohnuma, J. Suzuki, F. Wei, K. Tsuzaki, Direct observation of hydrogen trapped by NbC in steel using small-angle neutron scattering, Scripta Materialia 58 (2) (2008) 142–145.
[17] X. Zhou, D. Marchand, D.L. McDowell, T. Zhu, J. Song, Chemomechanical origin of hydrogen trapping at grain boundaries in fcc metals, Physical Review Letters 116 (7) (2016) 075502.
[18] Y. Chen, D. Haley, S.S. Gerstl, A.J. London, F. Sweeney, R.A. Wepf, W.M. Rainforth, P.A. Bagot, M.P. Moody, Direct observation of individual hydrogen atoms at trapping sites in a ferritic steel, Science 355 (6330) (2017) 1196–1199.
[19] Y. Chen, H. Lu, J. Liang, A. Rosenthal, H. Liu, G. Sneddon, I. McCarroll, Z. Zhao, W. Li, A. Guo, et al., Observation of hydrogen trapping at dislocations, grain boundaries, and precipitates, Science 367 (6474) (2020) 171–175.
[20] D. Jiang, E.A. Carter, First principles assessment of ideal fracture energies of materials with mobile impurities: implications for hydrogen embrittlement of metals, Acta Materialia 52 (16) (2004) 4801–4807.
[21] A. Alvaro, I.T. Jensen, N. Kheradmand, O. Løvvik, V. Olden, Hydrogen embrittlement in nickel, visited by first principles modeling, cohesive zone simulation and nanomechanical testing, International Journal of Hydrogen Energy 40 (47) (2015) 16892–16900.
[22] A. Tehranchi, X. Zhou, W. Curtin, A decohesion pathway for hydrogen embrittlement in nickel: Mechanism and quantitative prediction, Acta Materialia 185 (2020) 98–109.
[23] S. Bechtle, M. Kumar, B.P. Somerday, M.E. Launey, R.O. Ritchie, Grain-boundary engineering markedly reduces susceptibility to intergranular hydrogen embrittlement in metallic materials, Acta Materialia 57 (14) (2009) 4148–4157.
[24] M. Martin, B. Somerday, R. Ritchie, P. Sofronis, I. Robertson, Hydrogen-induced intergranular failure in nickel revisited, Acta Materialia 60 (6-7) (2012) 2739–2745.
[25] C. Beachem, A new model for hydrogen-assisted cracking (hydrogen embrittlement), Metallurgical and Materials Transactions B 3 (2) (1972) 441–455.
[26] H.K. Birnbaum, P. Sofronis, Hydrogen-enhanced localized plasticity-a mechanism for hydrogen-related fracture, Materials Science and Engineering A 176 (1-2) (1994) 191–202.
[27] T. Neeraj, R. Srinivasan, J. Li, Hydrogen embrittlement of ferritic steels: observations on deformation microstructure, nanoscale dimples and failure by nanovoiding, Acta Materialia 60 (13-14) (2012) 5160–5171.
[28] J. Song, W. Curtin, A nanoscale mechanism of hydrogen embrittlement in metals, Acta Materialia 59 (4) (2011) 1557–1569.
[29] J. Song, W. Curtin, Atomic mechanism and prediction of hydrogen embrittlement in iron, Nature materials 12 (2) (2013) 145–151.
[30] S.S. Shishvan, G. Csányi, V.S. Deshpande, Hydrogen induced fast-fracture, Journal of the Mechanics and Physics of Solids 134 (2020) 103740.
[31] R.L. Hayes, M. Ortiz, E.A. Carter, Universal binding-energy relation for crystals that accounts for surface relaxation, Physical Review B 69 (2004) 172104, doi:10.1103/PhysRevB.69.172104.
[32] M. Yamaguchi, M. Shiga, H. Kaburaki, Grain boundary decohesion by sulfur segregation in ferromagnetic iron and nickel a first-principles study, Materials transactions 47 (11) (2006) 2682–2689.
[33] T. Hajilou, I. Taji, F. Christien, S. He, D. Scheiber, W. Ecker, R. Pippan, V.I. Razumovskiy, A. Barnoush, Hydrogen-enhanced intergranular failure of sulfur–doped nickel grain boundary: In situ electrochemical micro-cantilever bending vs. dft, Materials Science and Engineering: A (2020) 139967.
[34] A. Van der Ven, G. Ceder, The thermodynamics of decohesion, Acta Materialia 52 (5) (2004) 1223–1235.

[35] R. Kirchheim, Hydrogen solubility and diffusivity in defective and amorphous metals, Progress in Materials Science 32 (4) (1988) 261–325.
[36] J. Song, M. Soare, W. Curtin, Testing continuum concepts for hydrogen embrittlement in metals using atomistics, Modelling and Simulation in Materials Science and Engineering 18 (4) (2010) 045003.
[37] G. Kresse, J. Furthmüller, Efficient iterative schemes for ab initio total-energy calculations using a plane-wave basis set, Physical Review B 54 (16) (1996) 11169.
[38] G. Kresse, D. Joubert, From ultrasoft pseudopotentials to the projector augmented-wave method, Physical Review B 59 (3) (1999) 1758.
[39] J.P. Perdew, K. Burke, M. Ernzerhof, Generalized gradient approximation made simple, Physical Review Letters 77 (18) (1996) 3865.
[40] P.E. Blöchl, Projector augmented-wave method, Physical Review B 50 (24) (1994) 17953.
[41] M. Methfessel, A. Paxton, High-precision sampling for brillouin-zone integration in metals, Physical Review B 40 (6) (1989) 3616.
[42] H.J. Monkhorst, J.D. Pack, Special points for brillouin-zone integrations, Physical review B 13 (12) (1976) 5188.
[43] A. van de Walle, G. Ceder, Automating first-principles phase diagram calculations, Journal of Phase Equilibria 23 (4) (2002) 348.
[44] A. Van De Walle, Multicomponent multisublattice alloys, nonconfigurational entropy and other additions to the alloy theoretic automated toolkit, Calphad 33 (2) (2009) 266–278.
[45] F. Körmann, A. Dick, B. Grabowski, T. Hickel, J. Neugebauer, Atomic forces at finite magnetic temperatures: Phonons in paramagnetic iron, Physical Review B 85 (12) (2012) 125104.
[46] B. Alling, F. Körmann, B. Grabowski, A. Glensk, I.A. Abrikosov, J. Neugebauer, Strong impact of lattice vibrations on electronic and magnetic properties of paramagnetic fe revealed by disordered local moments molecular dynamics, Physical Review B 93 (22) (2016) 224411.
[47] Z. Rák, D. Brenner, Ab initio investigation of the surface properties of austenitic Fe-Ni-Cr alloys in aqueous environments, Applied Surface Science 402 (2017) 108–113.
[48] C. Niu, A. Zaddach, A. Oni, X. Sang, J. Hurt, J. LeBeau, C. Koch, D. Irving, Spin–driven ordering of Cr in the equiatomic high entropy alloy NiFeCrCo, Applied Physics Letters 106 (16) (2015) 161906.
[49] O. Schneeweiss, M. Friák, M. Dudová, D. Holec, M. Šob, D. Kriegner, V. Holỳ, P. Beran, E.P. George, J. Neugebauer, et al., Magnetic properties of the CrMnFeCoNi high-entropy alloy, Physical Review B 96 (1) (2017) 014437.
[50] C. Niu, C.R. LaRosa, J. Miao, M.J. Mills, M. Ghazisaeidi, Magnetically-driven phase transformation strengthening in high entropy alloys, Nature Communications 9 (1) (2018) 1–9.
[51] J. Yamabe, K. Wada, T. Awane, H. Matsunaga, Hydrogen distribution of hydrogen-charged nickel analyzed via hardness test and secondary ion mass spectrometry, International Journal of Hydrogen Energy 45 (15) (2020) 9188–9199.
[52] G. Caskey, Effect of hydrogen on work hardening of type 304L austenitic stainless steel, Scripta Metallurgica 15 (11) (1981) 1183–1186, doi:10.1016/0036-9748(81)90294-5.
[53] C. San Marchi, T. Michler, K. Nibur, B. Somerday, On the physical differences between tensile testing of type 304 and 316 austenitic stainless steels with internal hydrogen and in external hydrogen, International Journal of Hydrogen Energy 35 (18) (2010) 9736–9745.
[54] M. Hatano, M. Fujinami, K. Arai, H. Fujii, M. Nagumo, Hydrogen embrittlement of austenitic stainless steels revealed by deformation microstructures and strain-induced creation of vacancies, Acta Materialia 67 (2014) 342–353.
[55] Y. Murakami, T. Kanezaki, Y. Mine, Hydrogen effect against hydrogen embrittlement, Metallurgical and Materials Transactions A 41 (10) (2010) 2548–2562.
[56] L. Zhang, Z. Li, J. Zheng, Y. Zhao, P. Xu, C. Zhou, C. Zhou, X. Chen, Dependence of hydrogen embrittlement on hydrogen in the surface layer in type 304 stainless steel, International Journal of Hydrogen Energy 39 (35) (2014) 20578–20584.
[57] T. Matsuo, J. Yamabe, S. Matsuoka, Y. Murakami, Influence of hydrogen and prestrain on tensile properties of type 316L austenitic stainless steel, Effect of hydrogen on materials. ASM International, Ohio (2009) 105–112.
[58] K. Ichii, M. Koyama, C.C. Tasan, K. Tsuzaki, Comparative study of hydrogen embrittlement in stable and metastable high-entropy alloys, Scripta Materialia 150 (2018) 74–77.